engineering proceedings

MDPI

*Proceeding Paper*

# Investigation of Natural Convection Heat Transfer in Two Vertical Heated Walls Partially Filled with Porous Media †

**Rana Nezar Dawood *, Ali L. Ekaid and Nabeel Sameer Mahmoud**

Air Conditioning and Refrigeration Engineering Department, College of Mechanical Engineering, University of Technology, Baghdad 10069, Iraq; ali.l.ekaid@uotechnology.edu.iq (A.L.E.); nabeel.s.mahmoud@uotechnology.edu.iq (N.S.M.)

* Correspondence: me.23.08@grad.uotechnology.edu.iq

† Presented at the 2nd International Conference on Engineering, Technology, and Applied Science Innovations (ICETASI 2026), Zakynthos, Greece, 24–26 September 2026.

**Abstract**

This study presents a comprehensive numerical and experimental investigation into natural convection heat transfer within two vertical heated parallel plates, comparing a clean air configuration against channels fully and partially filled with copper metal foam. The research characterizes the complex interplay between the enhancement provided by the foam's high surface area and the flow resistance introduced by Darcy–Forchheimer drag. For the porous regions, the Brinkman–Forchheimer extended Darcy model was employed under local thermal equilibrium (LTE) assumptions, while a low Reynolds number K-ε turbulence model was utilized to resolve high-buoyancy flows. The investigation spans Rayleigh numbers ($10^6$, $5 \times 10^6$, $10^7$, $5 \times 10^7$), porosity (0.85, 0.9, 0.95), and pore densities (10, 20, 30, 40). Results indicate that metal foam significantly augments thermal performance, with a porosity of 0.85 yielding an 87.3% enhancement over clean air at Ra = $5 \times 10^7$. One of the partial cases was identified as the optimal configuration for balancing thermal enhancement with reduced pressure drop. Notably, an inverse relationship was observed between pore density (PPI) and the Nusselt number, as higher PPI values significantly suppress fluid circulation.

**Keywords:** natural convection; porous metal foam; nusselt number

## 1. Introduction

The study of natural convection in vertical channels remains a cornerstone of thermal engineering, with extensive applications ranging from electronic cooling to solar energy harvesting. Research in this field has evolved from fundamental air-filled systems to complex configurations utilizing porous metal foams to enhance heat transfer. In the laminar regime, studies have focused on optimizing convective performance through geometric modifications. For air-filled vertical parallel plates, Olsson et al. [1] established validated analytical correlations for a wide Rayleigh number (Ra) range, while Salman et al. [2] and Lewandowski et al. [3] utilized experimental methods to demonstrate the significant impact of aspect ratio and channel width on the Nusselt number. The influence of non-parallel geometries was further explored by Shihab [4], who used the finite difference method (FDM) to show that converging vertical walls enhance convective flow for Ra between $10^2$ and $10^6$. Metal foams have emerged as effective thermal management materials due to their high porosity, large surface area, and thermal conductivity. Metal foams, often fabricated from aluminum or copper, can significantly alter flow structure and heat transfer characteristics

Check for updates

Academic Editor: Konstantinos Poirazidis

Published: 20 November 2026

**Copyright:** © 2026 by the authors. Licensee MDPI, Basel, Switzerland. This article is an open access article distributed under the terms and conditions of the Creative Commons Attribution (CC BY) license.

when introduced into a convective channel. The partial filling of vertical plates with porous metal foam offers a hybrid configuration, blending the benefits of enhanced conduction within the porous region and improved convective mixing in the clear fluid zones. In the context of porous metal foams, Andreozzi et al. [5] and Alhamdi et al. [6] investigated inclined and horizontal porous channels, highlighting the tradeoffs between foam-induced drag and surface area enhancement, while Uglah et al. [7] and Alsabery et al. [8] utilized specialized porous geometries, such as heat sinks with fin edges and square cavities, to confirm that the high thermal conductivity of metal foams provides a net improvement in thermal performance despite flow suppression. The transition to the turbulent regime represents a critical area of investigation for high-buoyancy scenarios where flow structures significantly alter heat transfer mechanisms. For air-filled channels, Anwar [9] and Badr et al. [10] investigated the onset of turbulence in vertical plates using Low Reynolds' number (LRN) K-ε models, noting that turbulence typically initiates in the thin boundary layers at $Ra > 10^5$. These findings were complemented by Yilmaz and Fraser [11], who explored asymmetric heating, and Pallares et al. [12], who provided high-fidelity data through direct numerical simulations (DNS). In porous media, the complexity increases due to the interaction between turbulent eddies and the solid matrix. Lauriat et al. [13] utilized the Brinkman–Forchheimer extended Darcy model to analyze these interactions at Ra up to $10^{12}$, demonstrating that neglecting inertial and viscous drag leads to an underprediction of velocity. Furthermore, Braga and De Lemos et al. [14] and Ekaid et al. [15] utilized macroscopic turbulence models to examine square porous cavities and localized heating, highlighting how the porous matrix dictates overall thermal performance through a balance of surface area and flow resistance. Studies utilizing the LTE assumption, such as Andreozzi et al. [5] and Alhamdi et al. [6], rely on the Brinkman–Forchheimer extended Darcy model to account for viscous and inertial drag while assuming a single temperature field. This non-Darcian approach was pioneered by Lauriat and Prasad [13], who established its necessity for accuracy at high Rayleigh numbers. Conversely, for high conductivity metal foams, researchers increasingly employ LTNE models to resolve separate energy equations for the solid and fluid phases. For instance, Uglah et al. [7] applied LTNE to optimize heat sinks, while Saeid et al. [16] and Alsabery et al. [8] used this framework to capture the complex thermal interactions in vertical plates and square cavities, respectively. Trilok, G et al. [17]. emphasize that while LTE may suffice in certain regimes, the LTNE model is essential for accurately characterizing the influence of pore density and porosity in convection-dominant scenarios. Previous reviews have addressed natural convection in either empty vertical plates or fully porous enclosers, but a focused synthesis on partially filled porous configurations remains limited. The unique interplay of conduction, convection, and flow obstruction in such systems poses significant modeling and experimental challenges. Furthermore, both laminar and turbulent flow regimes may be encountered depending on the Rayleigh number and the configuration of the porous medium. This paper aims to fill this gap via a numerical and experimental study that investigates natural convection between two vertical plates partially filled with porous metal foam. It discusses governing parameters, modeling approaches (non-Darcian, LTE), and methods (FVM, experimental setups). Emphasis is placed on comparative results, such as variations in Nusselt number, transition from laminar to turbulent flow, and the influence of foam configuration.

## 2. Experimental Study

### *2.1. The Flow Channels*

A channel is built to carry out the experimental part of this study. Air temperature measurement was made inside the channel at different elevations. Surface temperatures were also measured at the channel walls. The experimental setup comprised two identical

aluminum plates, each 70 cm long (L), 20 cm wide (W), and 0.5 cm thick (t). These were fixed to an iron structure that allowed the channel spacing (b) to be adjusted, maintaining the aspect ratio (L/b) of 10. Vertical plates were heated using nickel–chrome straps with a constant heat flux. Precision was maintained via a regulated power supply, voltage stabilizer, and fiberglass insulation (8 cm thick) to minimize heat loss. Temperature gradients were assessed using 20 type K thermocouples—10 embedded along the heated plate, and 10 within the fluid domain. These were connected to a selector switch and a digital thermometer reader for real-time monitoring.

### *2.2. The Experiments*

Air-only Recording: The experimental procedure commenced with the activation of the embedded electric heaters, which were regulated to ensure a uniform heat distribution across the plate surfaces. The system was monitored continuously until thermal equilibrium was established, ensuring that steady-state conditions were maintained for all subsequent measurements. Upon reaching this state, comprehensive data, including voltage, electrical current, and temperature, were recorded to characterize the natural convection heat transfer and flow dynamics. Finally, this experimental procedure was replicated across a range of power inputs to evaluate the influence of varying heat flux on the observed convective flow patterns.

Fully Filled Porous Material: In the experimental phase, assessing air temperature within a fully filled porous configuration, the copper metal foam samples were prepared by sizing the original (50 × 50 × 1) cm plates into (50 × 20 × 1) cm segments and assembling them as illustrated in Figure 1a. To facilitate accurate thermal monitoring, 10 thermocouples were secured at the midline between the plates using heat-resistant adhesive, while a top-mounted connector was employed to ensure structural stability and prevent assembly displacement. A 20 cm clearance was maintained at the base to accommodate unobstructed, free natural convection airflow. Following system stabilization, temperature data were recorded upon reaching thermal equilibrium, a process requiring between 8 and 12 h of continuous operation (Figure 1b).

Partially Filled Configurations

For the partially filled configurations, the metal foam plates were segmented into dimensions of (30 × 20 × 1) cm, (20 × 20 × 1) cm, and (10 × 20 × 1) cm to examine three distinct assembly patterns. Each arrangement maintained a 20 cm unobstructed air inlet at the base, followed by varied sequences of porous layers and air gaps (Table 1). Thermal measurements were recorded at the test section midline once steady-state conditions were achieved, a stabilization process necessitating 10 to 12 h of continuous operation per trial. This rigorous methodology ensured the acquisition of high-fidelity temperature distribution data, facilitating a robust analysis of natural convection heat transfer between vertical parallel plates across multiple power inputs and controlled experimental conditions (Figure 1c).

### *2.3. Uncertainty of the Experimental Data*

An uncertainty analysis is carried out to determine the level of uncertainty of the measurements. Typically, uncertainties are calculated to be 0.01 A for AC current, 0.3 V for voltage, 0.08 °C for the temperature flow, and 0.075 °C for the surface temperature. Typical relative errors for heat flux, heat transfer coefficient, and Nusselt number are 2.89%, 2.89%, and 2.88%, respectively. Details are given in [18,19].

**Table 1.** Partially filled arrangement.

| Configuration | Inlet Clearance | First Layer | Middle Layer | Top Layer | Experimental Procedure |
|---|---|---|---|---|---|
| Case A | 20 cm | 10 cm porous | 10 cm air | 30 cm porous | Continuous monitoring until thermal equilibrium is reached (10–12) hours. |
| Case B | 20 cm | 30 cm porous | 10 cm air | 10 cm porous | |
| Case C | 20 cm | 20 cm porous | 10 cm air | 20 cm porous | |

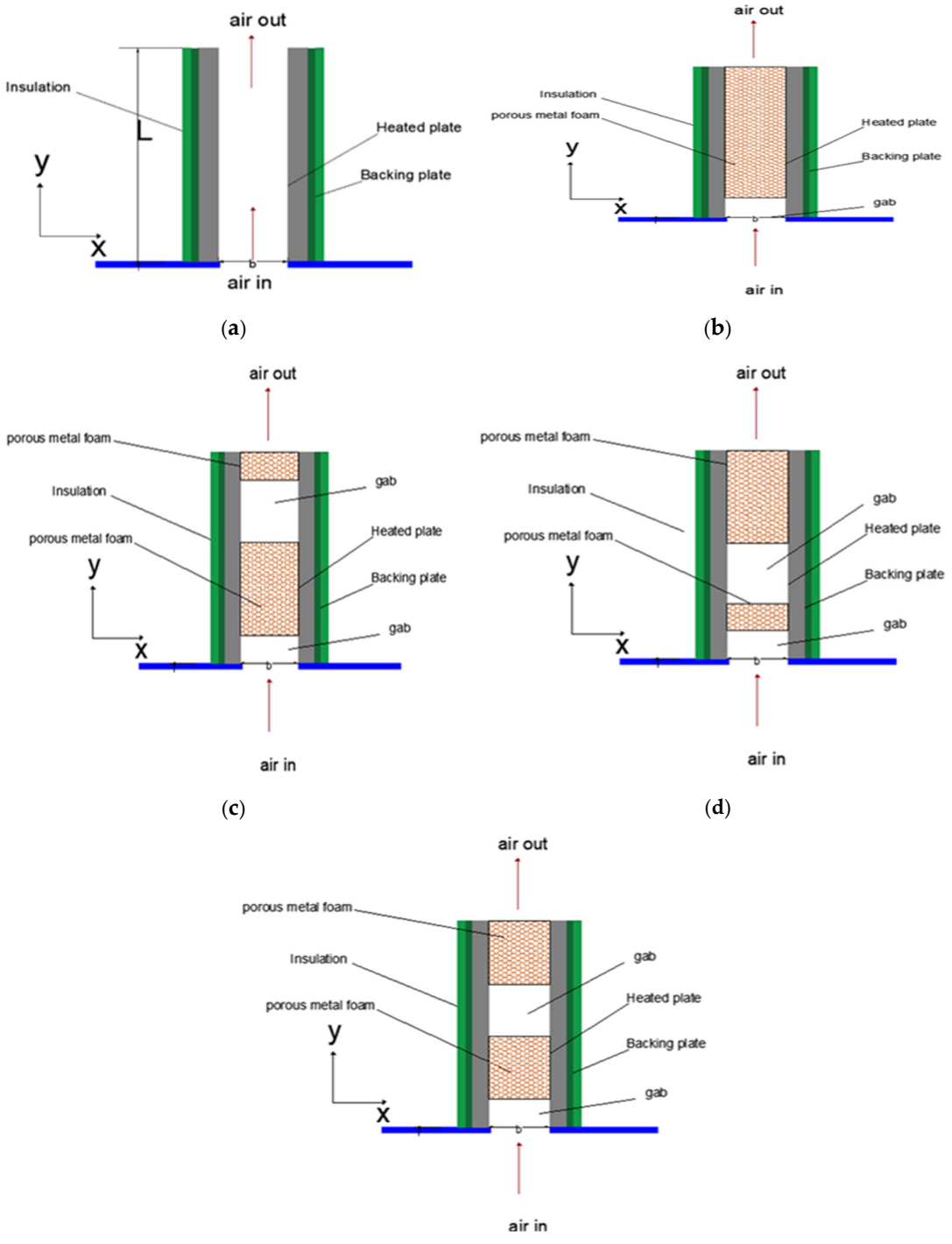



**Figure 1.** Experimental work configurations, (**a**) Geometry of parallel plates; (**b**) fully filled with metal foam; (**c**) partially filled with metal foam case A, (**d**) partially filled with metal foam case B, (**e**) partially filled with metal foam case C.

## 3. Numerical Study

Turbulent natural convection heat transfer and fluid flow inside the channel considered in this study have been simulated using the finite volume method-based commercial CFD code. The code is built using the LRN K-ε model.

### *3.1. Modeling Assumptions and Problem Formulation*

The porous medium is modeled as an isotropic, homogeneous, and solid open-cell copper metal foam with material properties as detailed in Table 2. The study is conducted within a two-dimensional domain under steady-state, incompressible, and turbulent flow conditions. The working fluid, air, is treated as a Newtonian fluid with constant thermodynamic properties, with the exception of density variations within the gravitational term, which are accounted for via the Boussinesq approximation. Furthermore, the fluid–solid interaction is governed by the no-slip condition and the assumption of local thermal equilibrium, and the system operates under a constant heat flux boundary condition, with the explicit exclusion of internal heat generation within the enclosure.

**Table 2.** Properties of the metal foam.

| | |
|---|---|
| Heat capacity | 385 J/Kg·K |
| Thermal conductivity | 400 W/m·K |
| Density | 8960 Kg/m$^3$ |
| Porosity | 95% |
| PPI | 20 |
| Plate dimensions | (50 × 50 × 1) cm |

### *3.2. Boundary Conditions*

The boundary conditions (Table 3) for the computational domain are defined to accurately reflect the physical constraints of the system. For the vertical walls, a constant heat flux is specified to model the thermal input at the plate surfaces, while a no-slip condition is enforced to assume zero fluid velocity, representing fluid adhesion to the wall. At the inlet (at y = 0), the system is constrained by ambient conditions, with pressure set to ambient pressure (Pi) and temperature (Ti) prescribed as ambient temperature. Correspondingly, the outlet (at y = L) is defined by an ambient pressure boundary (Po) (Figure 2a), while the temperature at both inflow and outflow boundaries may either be prescribed or left to evolve freely, depending on the specific requirements of the simulation to ensure accurate thermal and hydrodynamic representation of the flow.

1. Mass conservation equation [20]:

$$\frac{\partial \mathrm{u}}{\partial \mathrm{x}} + \frac{\partial \mathrm{v}}{\partial \mathrm{y}} = 0$$

2. The momentum equation in the x-direction. [21]:

$$\frac{\rho}{\varepsilon}\frac{\partial \mathrm{u}}{\partial \mathrm{t}} + \frac{\rho}{\varepsilon^2}\mathrm{u}\frac{\partial \mathrm{U}}{\partial \mathrm{x}} + \frac{\rho}{\varepsilon^2}\nu\frac{\partial \mathrm{u}}{\partial \mathrm{y}} = -\frac{\partial P}{\partial x} + \frac{1}{\varepsilon}\frac{\partial}{\partial x}\left[(\mu+\mu_t)\left(2\frac{\partial u}{\partial x}\right)\right] + \frac{1}{\varepsilon}\frac{\partial}{\partial y}\left[(\mu+\mu_t)\left(\frac{\partial u}{\partial y}+\frac{\partial v}{\partial x}\right)\right] - \eta(\frac{\mu}{k}u + \frac{C_f\rho}{k}u\sqrt{u^2+v^2})$$

3. The momentum equation in the Y-direction [21]:

$$\frac{\rho}{\varepsilon}\frac{\partial v}{\partial t} + \frac{\rho}{\varepsilon^2}u\frac{\partial \nu}{\partial x} + \frac{\rho}{\varepsilon^2}\nu\frac{\partial v}{\partial y} = -\frac{\partial P}{\partial y} + \frac{1}{\varepsilon}\frac{\partial}{\partial y}\left[(\mu+\mu_t)\left(2\frac{\partial \nu}{\partial y}\right)\right] + \frac{1}{\varepsilon}\frac{\partial}{\partial x}(\mu+\mu_t)\left[\left(\frac{\partial u}{\partial y}+\frac{\partial \nu}{\partial x}\right)\right] - \eta\left(\frac{\mu}{k}v + \frac{c_f\rho}{\sqrt{k}}\nu\sqrt{u^2+v^2}\right) + \rho g\beta(T-T_0)$$

where [22]

$$\mu_t = \rho c_\mu f_\mu \frac{k^2}{\varepsilon}$$

In the porous domain, $\eta = 1$, while in the clear air region, $\eta = 0$, $\varepsilon = 1$, and both the Darcy and Forchheimer resistance terms were omitted.

4. Thermal energy equation [21]:

$$\varepsilon + \frac{(1-\varepsilon)^{\rho} \mathrm{scP_s}}{\rho_f \mathrm{cp_f}} \frac{\partial T}{\partial t} + \left( u \frac{\partial T}{\partial x} + v \frac{\partial T}{\partial y} \right) = \left( \frac{k_{eff}}{cp} + \frac{\mu_t}{Pr} \right) \left[ \frac{\partial^2 T}{\partial x^2} + \frac{\partial^2 T}{\partial y^2} \right]$$

T is the local fluid temperature, and $k_{eff}$ can be calculated from [23]:

$$k_{eff} = \frac{\sqrt{2}}{2(R_A + R_B + R_C + R_D)}$$

where:

$$R_A = \frac{4d}{2e^2 + \pi d(1-e)(k_S - k_f) + 4k_f}$$

$$R_B = \frac{(e-2d)}{e^2(k_s - k_f) + 2k_f}$$

$$R_c = \frac{2\left(\sqrt{2} - 2e\right)}{\pi d^2 \sqrt{2}(k_S - 2k_f) + 2k_f}$$

$$R_D = \frac{2e}{e^2(k_s - k_f) + 4k_f}$$

$$d = \sqrt{\frac{\sqrt{8}(1-P) - \frac{3e^3}{2}}{\pi\left(3 - e\left(\sqrt{32}+1\right)\right)}}$$

$k_s$ is the thermal conductivity of the solid.
$k_f$ is the thermal conductivity of the fluid.
P is the porosity of the metal foam and e = 0.198.
For $\varepsilon = 0$ $k_{eff} = k_s$ and for $\varepsilon = 1$ $k_{eff} = k_f$.

5. Turbulent kinetic energy equation:

$$\rho \frac{\partial k}{\partial t} + \rho_u \frac{\partial k}{\partial x} + \rho_v \frac{\partial k}{\partial y} = \frac{\partial}{\partial x}\left[ \left( \mu + \frac{\mu_t}{\sigma_k} \right) \frac{\partial k}{\partial x} \right] + \frac{\partial}{\partial y}\left[ \left( \mu + \frac{\mu_t}{\sigma_k} \right) \frac{\partial k}{\partial y} \right] + P_k + G_k - \rho\varepsilon + D$$

$$\rho \frac{\partial \varepsilon}{\partial t} + \rho u \frac{\partial \varepsilon}{\partial x} + \rho v \frac{\partial \varepsilon}{\partial y} = \frac{\partial}{\partial X}\left[ \left( \mu + \frac{\mu_t}{\sigma_\varepsilon} \right) \frac{\partial \varepsilon}{\partial x} \right] + \frac{\partial}{\partial y}\left[ \left( \mu + \frac{\mu_t}{\sigma_\varepsilon} \right) \frac{\partial \varepsilon}{\partial y} \right] + \frac{\varepsilon}{k}\left( C_{\varepsilon_1} f_1 P_k + C_{\varepsilon_1} G_k - C_{\varepsilon_2} f_2 \rho_\varepsilon \right)$$

$$P_k = \mu_t \left[ 2\left( \frac{\partial u}{\partial x} \right)^2 + 2\left( \frac{\partial v}{\partial y} \right)^2 + \left( \frac{\partial u}{\partial y} + \frac{\partial v}{\partial x} \right)^2 \right]$$

$$G_k = -\frac{\mu_t}{\sigma_t} g\beta \frac{\partial T}{\partial y}$$

Equation for the rate of energy dissipation:

$$\rho \frac{\partial \varepsilon}{\partial t} + \rho u \frac{\partial \varepsilon}{\partial x} + \rho v \frac{\partial \varepsilon}{\partial y} = \frac{\partial}{\partial x}\left[ \left( \mu + \frac{\mu_t}{\sigma_\varepsilon} \right) \frac{\partial \varepsilon}{\partial x} \right] + \frac{\partial}{\partial y}\left[ \left( \mu + \frac{\mu_t}{\sigma_\varepsilon} \right) \frac{\partial \varepsilon}{\partial y} \right] + \left( c_{\varepsilon_1} f_1 (P_k + c_{\varepsilon_3} G_k) - \rho c_{\varepsilon_3} f_2 \varepsilon \right) \frac{\varepsilon}{k} + E$$

E is a term that occurs when low Reynolds number turbulence models are used. $\sigma\varepsilon$ is the turbulent Prandtl number for $\varepsilon$.

$$E = \rho\mu \left\{ \left( \frac{\partial^2 U}{\partial X^2} \right)^2 + \left( \frac{\partial^2 U}{\partial Y^2} \right)^2 + \left( \frac{\partial^2 V}{\partial X^2} \right)^2 + \left( \frac{\partial^2 V}{\partial Y^2} \right)^2 + 2\left[ \left( \frac{\partial^2 U}{\partial X \partial Y} \right)^2 + \left( \frac{\partial^2 V}{\partial X \partial Y} \right)^2 \right] \right\}$$

https://doi.org/10.3390/engproc2026167024

6. Modification for low Reynolds number models (Yang–Shih) [24,25].

$$D = 0.0,\ C\varepsilon_1 = 1.44,\ C\varepsilon_2 = 1.92,\ C\varepsilon_3 = \mathrm{Tanh}\frac{v}{u},$$

$$\sigma_k = 1.0,\ \sigma_\varepsilon = 1.3\ f_1 = f_2 = \frac{Re_t^{0.5}}{\left(1 + Re_t^{0.5}\right)},$$

$$f_\mu = \left[\mathrm{Re_y} - 5 \times 10^{-7}\mathrm{Re_y^3} - 10^{-10}\mathrm{Re_y^5}\right]^{0.5}\left(1 + \mathrm{Re_t^{0.5}}\right)$$

Pore diameter from [26].

$$d_P = (-0.921\ln(PPI) + 5.3564)10^{-3}$$

Permeability (K) from [27]

$$\frac{d_f}{dp} = 1.18\sqrt{\frac{(1-\epsilon)}{3\pi}\frac{1}{G}}$$

where G

$$G = 1 - e^{-\frac{(1-\epsilon)}{0.04}}$$

The permeability will be calculated from [28]

$$\frac{k}{d_p^2} = 0.00073(1-\epsilon)^{-0.224}\left(\frac{d_f}{d_P}\right)^{-1.11}$$

And Inertial (Forchheimer) coefficient (Cf) from [27]:

$$c_f = 0.00212(1-\epsilon)^{-0.123}\left(\frac{d_f}{dp}\right)^{-1.63}$$

Non-dimensional equations

$$X = \frac{x}{b},\ Y = \frac{y}{b},\ U = \frac{ub}{\sqrt{\frac{g\beta q'' b^2}{k_f}}},\ V = \frac{v_b}{\sqrt{\frac{g\beta q'' b^2}{k_f}}},\ \theta = \frac{k_f(T - T_\infty)}{q'' b},$$

$$Ra = \frac{\rho^2 g \beta_q'' b^4}{k_f \mu^2} p_r,\ Da = \frac{k_f}{b^2},\ Nu_x = \frac{q'' b}{k_f(Ts - To)} = \frac{1}{\theta_x}, \overline{Nu} = \frac{L}{b_0}\int_N^{L/b} Nu_x dx$$

**Table 3.** Boundary conditions for computational domain.

| Boundary Conditions | U | V | T | K | ε |
|---|---|---|---|---|---|
| AB & LK | $\partial U/\partial X = 0$ | $V = 0$ | $\partial T/\partial X = 0$ | $\partial K/\partial X = 0$ | $\partial \varepsilon/\partial X = 0$ |
| EF & GH | $\partial U/\partial X = 0$ | $V = 0$ | $T = 0$ | $\partial K/\partial X = 0$ | $\partial \varepsilon/\partial X = 0$ |
| FG | $U = 0$ | $\partial V/\partial Y = 0$ | $T = 0$ | $\partial K/\partial Y = 0$ | $\partial \varepsilon/\partial Y = 0$ |
| AL | $U = 0$ | $\partial V/\partial Y = 0$ | $\partial T/\partial Y = 0$ | $\partial K/\partial Y = 0$ | $\partial \varepsilon/\partial Y = 0$ |
| CD | $U = 0$ | $V = 0$ | $T_w = T_{w+1} + \frac{\Delta x q''}{k_{eff}}$ | $K = 0$ | $\varepsilon_w = \frac{\mu}{\rho}\left(\frac{\partial^2 k}{\partial x^2}\right)$ |
| IJ | $U = 0$ | $V = 0$ | $T_w = T_{w+1} + \frac{\Delta x q''}{k_{eff}}$ | $K = 0$ | |
| BC, DE, JK | $U = 0$ | $V = 0$ | $\partial T/\partial Y = 0$ | $K = 0$ | |

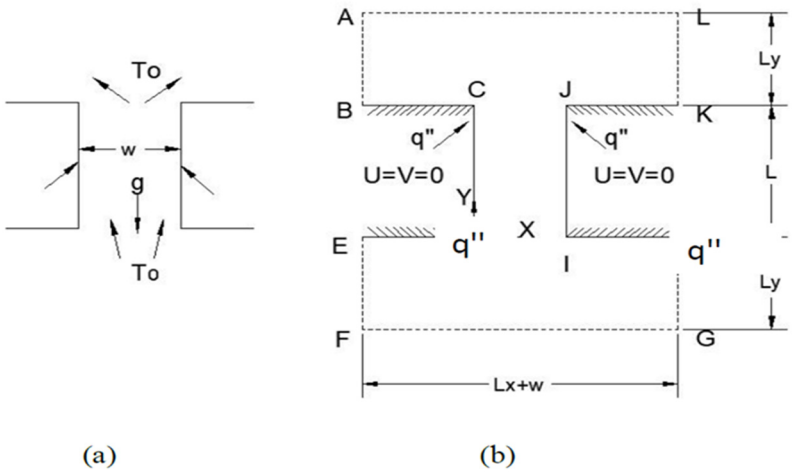



**Figure 2.** Problem schematic: (**a**) flow diagram; (**b**) computational domain.

### *3.3. Numerical Method*

The program utilizes a simple algorithm for pressure–velocity coupling and implements a staggered grid system to ensure numerical stability, where velocity components (u, v) are calculated at control volume faces while scalar variables (T, p, K, ε) are resolved at main grid points. Discretization is achieved through a combination of central difference and hybrid schemes, which are then solved using the line successive over relaxation (LSOR) technique and the tridiagonal matrix algorithm (TDMA) in a line-by-line iterative process. The code is modularly structured with specialized subroutines. A PROPS module was used to manage fluid properties such as eddy viscosity.

## 4. Results and Discussion

This study considers the aspect ratio (L/b = 10), Rayleigh number ($5 \times 10^7$), and porosity (ε = 0.9) as crucial parameters. By examining the effects of these parameters, numerical simulations are utilized to understand the flow behavior, velocity distribution, and temperature profiles. The impact of porous media on the natural convection was investigated across four distinct configurations, comparing a fully filled case with three partially filled arrangements: case A (10 cm porous, 10 cm air, and 30 cm porous), case B (30 cm porous, 10 cm air, and 10 cm porous), and case C (20 cm porous, 10 cm air, and 20 cm porous). The study evaluated the Local and average Nusselt number, variations in porosity and pore density (PPI), and Rayleigh number to characterize the influence of porous metal foam in enhancing heat transfer.

### *4.1. Temperature Contours*

The numerical investigation of natural convection shown in Figure 3 reveals distinct thermal behaviors governed by the spatial distribution of the porous medium. In the fully filled configuration, the isotherms remain, in general, horizontal and parallel throughout the channel, signifying a conduction-dominated regime where the porous matrix effectively allows a convective flow. Conversely, the partially filled configurations (cases A, B, and C) demonstrate a transition to a convection-dominated state characterized by a central, thermally uniform core and significant isotherm curvature near the vertical walls. While the fully filled case maintains a moderate peak temperature of $\theta = 0.136$, the partially filled case A represents a moderate convective state with a peak temperature of $\theta = 0.149$, displaying a well-mixed central core but less intense boundary gradients than case C. Case B achieves the most effective overall heat distribution, resulting in the lowest peak temperature

$\theta = 0.134$ and a large, thermally uniform green zone that suggests high convective mixing. Finally, case C exhibits the most extreme thermal stratification, reaching the highest peak temperature of $\theta = 0.152$. This configuration traps heat at the top of the enclosure.

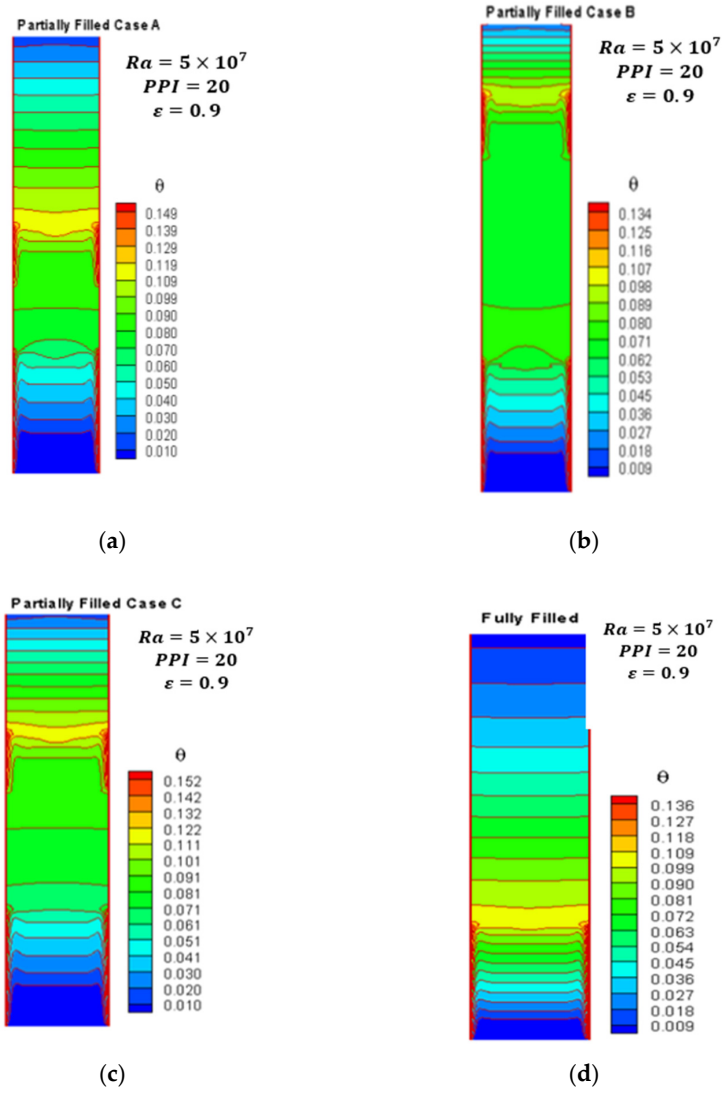



**Figure 3.** Temperature contour for a partially and fully filled channel with porous metal foam: (**a**) partially filled case A; (**b**) partially filled case B; (**c**) partially filled case C; (**d**) Fully filled.

### *4.2. Velocity Contours*

The velocity profiles in Figure 4 illustrate a fundamental compact between heat transfer surface area and flow resistance under buoyancy-driven conditions. In the fully filled case, the air faces continuous Darcy–Forchheimer resistance, leading to a restricted but uniform velocity distribution that maximizes contact time but minimizes the total mass flow. Conversely, cases A, B, and C, where case A provides a surface area by placing a thin 10 cm porous block, ensures the air is moving at a higher velocity before it hits the main heat exchange surface. The resistance of the foam helps redistribute the air, preventing air from moving near the center only. By the time the air reaches the 30 cm upper block, it has already gained momentum in the 10 cm clear gap. In case B, the internal configuration of the porous blocks is inverted relative to case A; the velocity vector indicates that the primary flow resistance is shifted toward the bottom of the channel, which forces the air to overcome a significant pressure drop early in its development, which can potentially lead to

a more uniform velocity distribution but may also dampen the overall flow rate compared to a top-heavy configuration. The 10 cm gap serves as a redevelopment zone where the air can recover some momentum before passing through the final 10 cm block. This exit block serves to maintain a thermal contact at the end of the channel. In case C, the vertical channel is configured with a symmetrical distribution of porous blocks, consisting of 20 cm porous blocks at the entry and exit and 10 cm intermate air gap; the velocity vectors reveal that the first 20 cm block initiates a pressure drop early in the flow development, while the 10 cm gap provides a re-acceleration zone where the air can recover momentum before entering the final 20 cm. This arrangement results in a more uniform distribution across the plates.

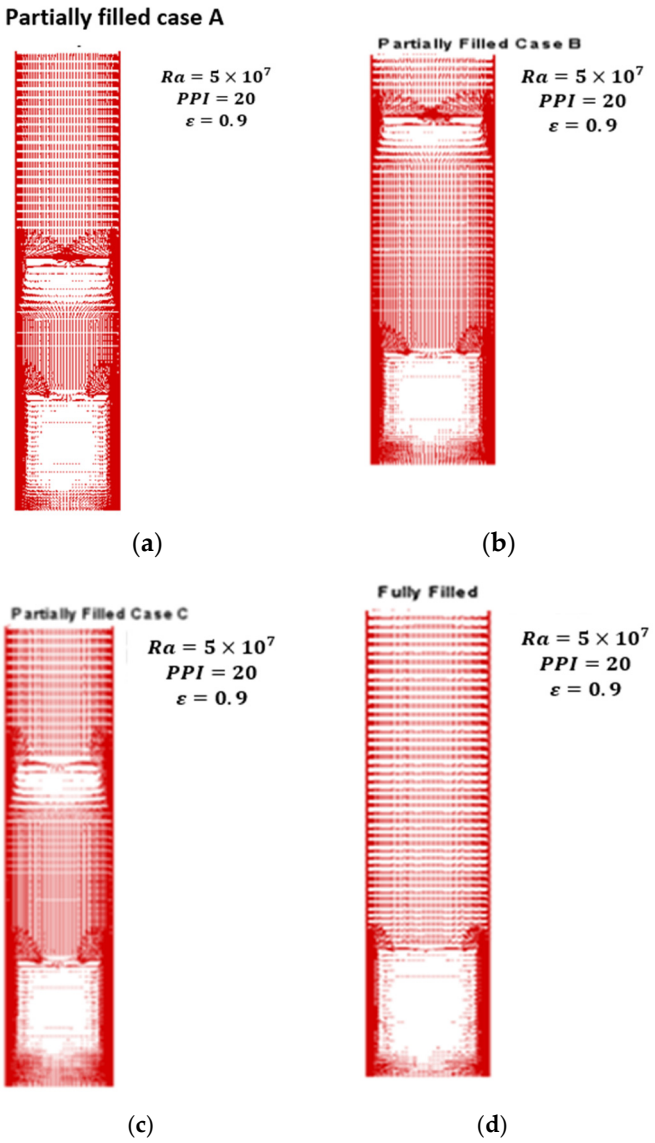



**Figure 4.** Velocity contour for a partially and fully filled channel with porous metal foam: (**a**) partially filled case A; (**b**) partially filled case B; (**c**) partially filled case C; (**d**) Fully filled.

### *4.3. Effect of Rayleigh Number on Local Nusselt Number for Air*

Figure 5 compares the current experimental data and numerical simulations with the established correlation by Cohen etc. [29]. The graph shows a consistent upward trend, where increasing the Rayleigh number enhances the overall convective heat transfer across the plates. The close proximity of the numerical curve and the experimental data point to

the existing literature, demonstrating high accuracy in the current model, and the close agreement between the simulation and the literature benchmark proves that the numerical model accurately captures the physical behavior of the system. While the experimental data points sit slightly lower at higher Rayleigh numbers due to heat losses, the overall enhancement for the experimental data as the Ra number increases is 91.7%.

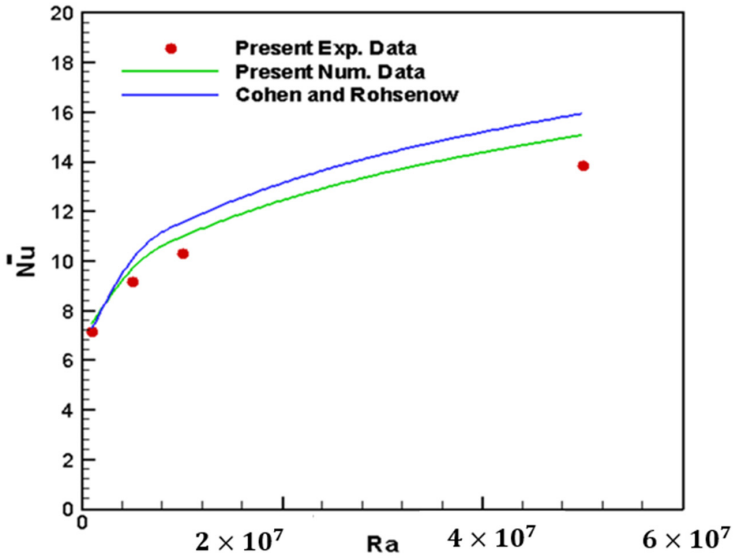



**Figure 5.** Effect of Rayleigh number on average Nusselt number for air.

### *4.4. Effect of Porosity on Average Nusselt Number for Fully Filled Case*

The relationship between the average Nusselt number and the Rayleigh number has been illustrated in Figure 6. Across all cases, the heat transfer performance improves as the Rayleigh number increases. Lower porosity levels ($\varepsilon = 0.85$) result in a higher Nusselt number because the denser metal matrix provides a greater surface area for heat exchange compared to higher porosity levels, like $\varepsilon = 0.95$. While all foam-filled configurations outperform the empty channel baseline, the experimental data ($\varepsilon = 0.95$) show a lower heat transfer rate than the numerical predictions at a high Rayleigh number. This deviation is likely due to the physical flow resistance and pressure drop inherent in the foam structure. At Ra $=5 \times 10^7$, the introduction of porous medium with $\varepsilon = 0.85$ enhances the heat transfer by approximately 87.3% compared to the clean fluid (air) case, while reducing the porosity from the experimental state ($\varepsilon = 0.95$) to a denser structure ($\varepsilon = 0.85$) results in an enhancement of approximately 45.6%.

### *4.5. Effect of Pore Density (PPI) on Average Nusselt Number for Fully Filled Case*

The provided Figure 7 illustrates the variation of the average Nusselt number as a function of PPI for a fully filled porous medium with constant porosity of $\varepsilon = 0.9$ at two distinct Rayleigh numbers. A consistent downward behavior is observed across the sampled range, indicating that an increase in PPI—which corresponds to a reduction in individual pore size—suppresses convective heat transfer. This degradation in average Nusselt number is likely attributable to the increased flow resistance associated with denser pore structures, which inhibit fluid circulation. Furthermore, the plot highlights a strong dependency on the Rayleigh number, as the Ra $= 5 \times 10^7$ case maintains significantly higher heat transfer rates compared to the Ra $= 10^7$ case, though both remain sensitive to the geometric constraints imposed by the porous matrix. For a structure with 10 PPI, increasing the Rayleigh number from $10^7$ to $5 \times 10^7$ results in a heat transfer enhancement of

approximately 96.3%. This demonstrates that, at lower pore densities, the system is highly sensitive to increases in buoyancy-driven convection, nearly doubling the Nusselt number.

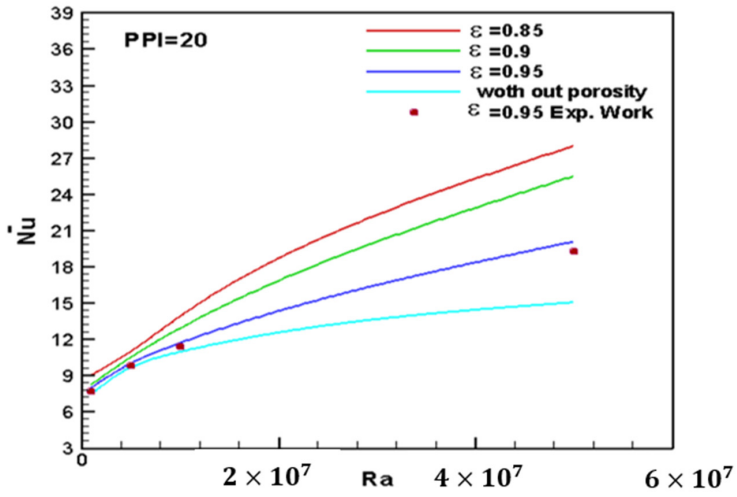



**Figure 6.** Effect of porosity on the average Nusselt number for a fully filled channel with porous metal foam.

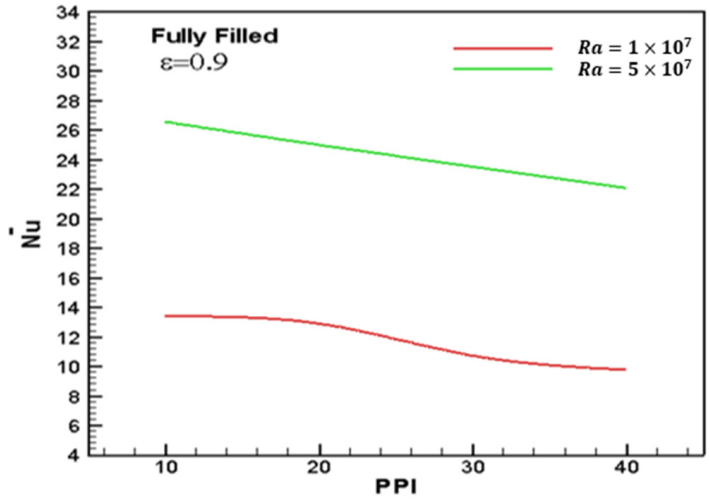



**Figure 7.** Effect of PPI on the average Nusselt number for fully filled channel with porous metal foam.

### *4.6. Effect of Porosity on Average Nusselt Number*

The results in Figure 8 indicate that the inclusion of porous metal foam enhances the heat transfer rate, as evidenced by the higher average Nusselt numbers across all porous configurations compared to the clean air. Among the partially filled cases, case B demonstrates the superior thermal performance, maintaining the highest average Nusselt numbers across the entire investigated porosity range. This enhanced performance in case B is due to the strategic distribution of the porous material that provides more effective surface area for heat exchange compared to cases A and C. Furthermore, case B exhibits a relatively stable heat transfer profile with increasing porosity, indicating a powerful design that maintains thermal enhancement. In the fully filled configuration, the porous occupies the entire domain, meaning the fluid is subjected to the drag forces of the enhanced surface area of the solid. Consequently, even a small increase in porosity causes a global reduction in the available heat exchange surface, leading to the sharp decline in average Nusselt numbers observed in the figure. Conversely, the partially filled cases exhibit flatter slopes

because the porosity is localized. In these cases, a significant portion of the fluid can bypass the porous zones through clear fluid regions of lower resistance. At a porosity of 0.85, the data show case B provides an improvement over cases A and C, with enhancements of 4.7% and 2.5%, respectively.

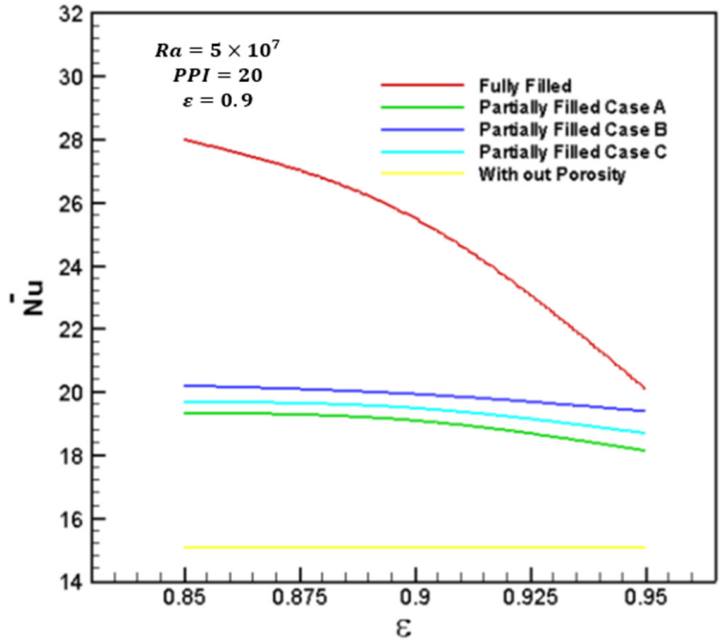



**Figure 8.** Effect of porosity on average Nusselt number.

### *4.7. Effect of Pore Density (PPI) on Average Nusselt Number*

The provided Figure 9 represents the dependence of the average Nusselt number on pore density (PPI) for a buoyancy-driven convective system at Ra = $5 \times 10^7$ and ε = 0.9. A comparative analysis reveals that the fully filled configuration yields the most significant thermal enhancement. A pervasive inverse correlation is observed across all cases. As the PPI increases from 10 to 40, the Nusselt number exhibits a monotonic decline. This suggests that while the introduction of porous enhances heat transfer by increased surface area and improved thermal dispersion, the flow resistance at higher pore densities becomes the dominant factor. Specifically, higher PPI values correspond to reduced permeability, which increases the pressure drop and suppresses the velocity of the flow. Among the partially filled configurations, case B demonstrates superior thermal performance, indicating that the strategic optimization of the porous insert can lessen the resistance while maximizing convective heat transfer. AT 10 PPI, case B provides 10.4% enhancement over case A and 5.5% over case C. This indicates that the arrangement of case B creates a more favorable environment for convective heat transfer compared to cases A and C.

### *4.8. Experimental Work*

Figure 10 demonstrates the average Nusselt number $(\overline{Nu})$ as a function of the Rayleigh number (Ra). There was a positive correlation across all configurations, confirming that enhanced buoyancy forces correlate with increased convective heat transfer efficiency. Among the investigated cases, the fully filled case exhibits superior $(\overline{Nu})$ values, attributed to the maximized surface area and enhanced conduction pathways provided by the full-volume metal matrix, while the various partially filled cases (A, B, and C) reflect tradeoffs between thermal enhancement and flow resistance. Furthermore, the close alignment between the numerical lines and experimental markers validates the employed computational model,

with the high degree of agreement—most notably in partially filled case C—suggesting that the model effectively captures the physical phenomena governing these specific configurations. Regarding the relative error between the numerical work ($\overline{N}u_{num.}$) and the experimental results ($\overline{N}u_{exp.}$), the error percentage is found to be 4.1% for the fully filled case, and (5.2%, 2.7%, and 0.5%) for the partially filled cases (A, B, and C), respectively.

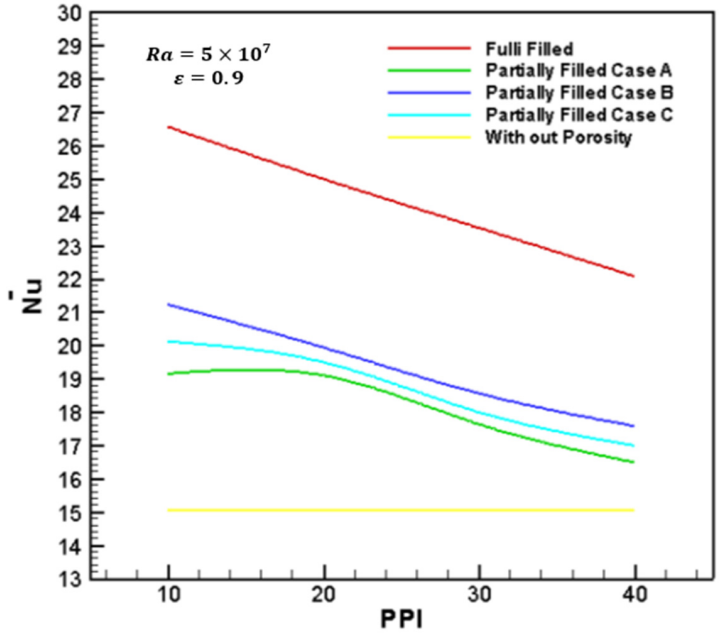



**Figure 9.** Effect of pore density (PPI) on average Nusselt number.

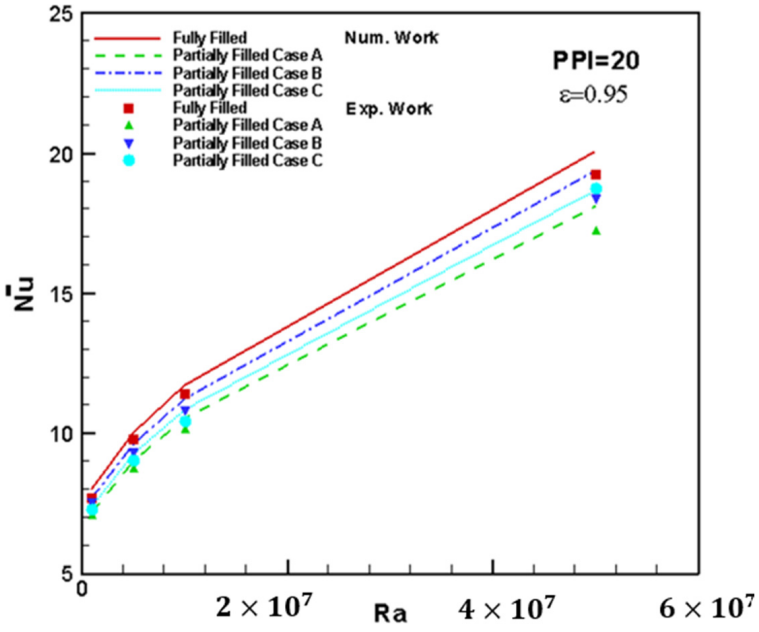



**Figure 10.** Comparison of the numerical and experimental study of the effect of Ra number on Nu number for partially and fully filled cases.

### *4.9. Numerical Validation*

When comparing the recent numerical work with [30] Marcondes F, in Figure 11, which represents natural convection in porous medium using a model ($\varepsilon = 0.4$, $Ra_m = 5 \times 10^3$, $Da = 10^{-6}$, $A = 1$, and $R_k = 1$), Figure 11a,c demonstrate that the thermal field maintains

a consistent isothermal structure, characterized by buoyancy-induced gradients that promote steady heat transfer from the heated vertical wall to the cooled one. Figure 11b,d substantiate this by presenting a stable, unified vortex flow pattern, which prevents the formation of localized high-velocity channels near the boundaries. In this configuration, the natural convection process is governed purely by the interaction between buoyancy forces and the consistent resistance offered by the porous medium, as modeled by the Darcy–Brinkman–Forchheimer terms. These figures illustrate a baseline scenario where the convective flow and thermal stratification are entirely predictable, establishing that flow structure serves as the fundamental mechanism for heat transport in the non-Darcian environment, with good agreement between the recent work and the literature.

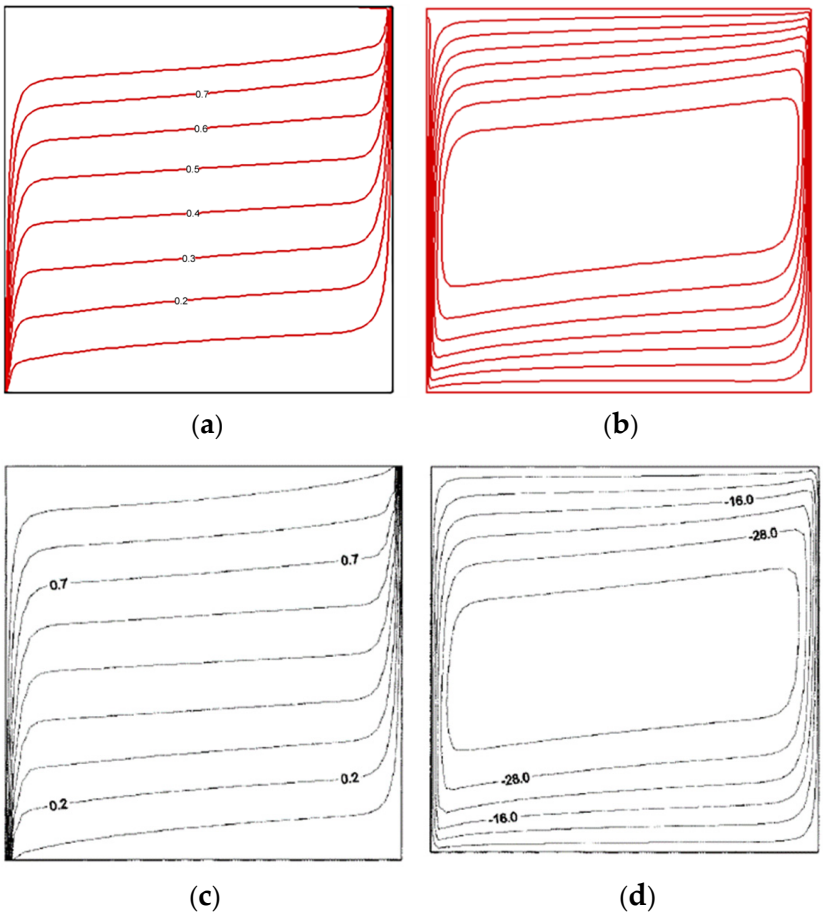



**Figure 11.** Isothermal and streamlines comparing recent work (**a**,**b**) with the literature [30], for $\varepsilon = 0.4$, $Ra_m = 5 \times 10^3$, Da= $10^{-6}$, A = 1, and $R_k = 1.$, (**a**,**b**) recent work, (**c**,**d**) Reproduced from [30], Emerald Group Publishing Limited: 2006.

## 5. Conclusions

This study investigates the influence of partially filled porous metal foam inserts on natural convection heat transfer between vertical parallel plates, comparing a clear-air baseline against both fully and partially filled configurations. The findings demonstrate that integrating porous metal foam significantly augments heat transfer due to the high thermal conductivity of the metallic matrix and the expanded surface area available for fluid–solid thermal interaction. Across all arrangements, an increase in the Rayleigh number from $10^6$ to $5 \times 10^7$ consistently yields higher average Nusselt numbers, as intensified buoyancy forces accelerate fluid circulation, reduce thermal boundary layer thickness, and facilitate more efficient heat dissipation. While the fully filled case achieves the greatest thermal enhance-

ment, it also imposes the highest flow resistance. Among the partially filled arrangements, the configuration featuring a 30 cm porous section at the inlet (case B) proved most efficient by balancing performance optimization with reduced pressure drop. Furthermore, the analysis reveals an inverse relationship between porosity and the Nusselt number, as lower porosity provides a denser matrix and superior effective thermal conductivity. The results also indicate that lower PPI values are more effective for natural convection, as excessive PPI increases flow resistance and reduces permeability to a degree that undermines convective efficiency.

**Author Contributions:** Conceptualization, R.N.D. and A.L.E.; methodology, R.N.D. and A.L.E.; investigation, R.N.D. and A.L.E.; writing—review and editing, R.N.D., A.L.E. and N.S.M. All authors have read and agreed to the published version of the manuscript.

**Funding:** This research received no external funding.

**Institutional Review Board Statement:** Not applicable.

**Informed Consent Statement:** Not applicable.

**Data Availability Statement:** The data supporting the findings of this study are available from the corresponding author upon reasonable request.

**Conflicts of Interest:** The authors declare no conflicts of interest.

## Abbreviations

| Symbol | Description | Unit |
|---|---|---|
| c | Specific heat of fluid | kJ/kg·K |
| C | Form drag coefficient | $m^{-1}$ |
| T | Thickness of model or foam | cm |
| K | Thermal conductivity | W/m·K |
| κ | Permeability | $m^2$ |
| L | Length of model or foam in flow direction | cm |
| $q''$ | Heat flux | $W/m^2$ |
| T | Temperature | °C |
| $u$ | Velocity in x- direction | m/s |
| $v$ | Velocity in the y-direction | m/s |
| U | Dimensionless velocity in the x–direction | |
| V | Dimensionless velocity in the y–direction | |
| W | Width of model or metal foam | cm |
| x | Axial coordinate along the flow direction | |
| y | Coordinate perpendicular to flow direction | |
| cp | Specific heat | j/kg·K |
| $C_1$, $C_2$, $C_3$, $C_\mu$ | Coefficients of k-ε model | |
| CD | Drag coefficient through porous media | |
| $C_f$ | Inertial (Forchheimer) coefficient | |
| $d_f$ | Fiber diameter | m |
| $k_{eff}$ | Effective thermal conductivity | w/m·k |
| g | Gravitational acceleration | $m/s^2$ |
| b | Characteristic length | cm |
| $T_f$ | Mean film air temperature | °C |
| $d_P$ | Pore Diameter | |
| $T_\infty$ | Ambient entrance temperature | |
| $T_0$ | Temperature of air in the case of with and without porous | |
| t | time | |
| $R_k$ | Thermal conductivity ratio between medium and fluid | |
| A | Aspect ratio | |
| LTNE | Local thermal none equilibrium | |
| LTE | Local thermal equilibrium | |
| α | Thermal diffusivity | $m^2/s$ |

| | | |
|---|---|---|
| $\beta$ | Thermal expansion coefficient | 1/k |
| ε | Porosity | |
| $\theta$ | Dimensionless temperature | |
| $\sigma$ | Effective Prandtl number | |
| $\mu$ | Dynamic viscosity | Kg/m·s |
| $\mu_t$ | Turbulent Dynamic viscosity | Kg/m·s |
| ρ | Density | $Kg/m^3$ |

**Dimensionless Group**

| **Symbol** | **Definition** |
|---|---|
| Pr | Prandtl number =Rate of momentum to thermal diffusivities = υ/α |
| Gr | Grashof number = Rate of buoyancy to viscosity forces = $\frac{g\beta q'' b^4}{k\nu^2}$ |
| Ra | Rayleigh number = $\frac{g\beta\rho^2 q'' b^4}{k\mu^2}$ |
| Da | Darcy number = effect of permeability to characteristic length = $k/b^2$ |

## References


1. Olsson, C.-O. Prediction of Nusselt Number and Flow Rate of Buoyancy Driven Flow Between Vertical Parallel Plates. *J. Heat Transf.* **2004**, *126*, 97–104. [CrossRef]
2. Salman, Y.K.; Hamad, H.S. Laminar natural convection heat transfer between ducted parallel plates. *J. Eng.* **2008**, *14*, 2786–2803. [CrossRef]
3. Lewandowski, W.M.; Ryms, M.; Denda, H. Natural convection in symmetrically heated vertical channels. *Int. J. Therm. Sci.* **2018**, *134*, 530–540. [CrossRef]
4. Shihab, S.H.; Ekaid, A.L.; Alsaedi, H.M. Experimental investigation of natural convection in a vertical convergent plate. *AIP Conf. Proc.* **2025**, *3211*, 040012. [CrossRef]
5. Andreozzi, A.; Bianco, N.; Iasiello, M.; Naso, V. Natural convection in a vertical channel with open-cell foams. *J. Phys. Conf. Ser.* **2020**, *1599*, 012013. [CrossRef]
6. Alhamdi, S.F.H.; Al-Azawii, M.M.S.; Alshara, A.K. Cooling High Power Microchip Using Metallic Porous Heat Sink. *Diyala J. Eng. Sci.* **2025**, 103–119. [CrossRef]
7. Uglah, A.M.; Jubear, A.J. Numerical thermal performance of free convection in metal foam heat sinks with fin edges. *Univ. Thi-Qar J. Eng. Sci.* **2020**, *11*, 19–30. [CrossRef] [PubMed]
8. Alsabery, A.; Saleh, H.; Arbin, N.; Hashim, I. Unsteady natural convection in a square cavity partially filled with porous media using a thermal non-equilibrium model. *Int. J. Math. Comput. Phys. Quantum Eng.* **2015**, *9*, 2–7.
9. Anwar, S. Natural Convection Flow in Parallel-Plate Vertical Channels. Master's Thesis, King Fahd University of Petroleum and Minerals, Dhahran, Saudi Arabia, 2003.
10. Badr, H.M.; Habib, M.A.; Anwar, S.; Ben-Mansour, R.; Said, S.A.M. Turbulent natural convection in vertical parallel-plate channels. *Heat Mass Transf.* **2006**, *43*, 73–84. [CrossRef]
11. Yilmaz, T.; Fraser, S.M. Turbulent natural convection in a vertical parallel-plate channel with asymmetric heating. *Int. J. Heat Mass Transf.* **2007**, *50*, 2612–2623. [CrossRef]
12. Pallares, J.; Fabregat, A.; Lei, C. Direct numerical simulation of the fully developed turbulent free convection flow in an asymmetrically heated vertical channel. *Int. J. Therm. Sci.* **2023**, *191*, 108352. [CrossRef]
13. Lauriat, G.; Prasad, V. Non-Darcian effects on natural convection in a vertical porous enclosure. *Int. J. Heat Mass Transf.* **1989**, *32*, 2135–2148. [CrossRef]
14. Braga, E.J.; de Lemos, M.J. Turbulent natural convection in a porous square cavity computed with a macroscopic κ–ε model. *Int. J. Heat Mass Transf.* **2004**, *47*, 5639–5650. [CrossRef]
15. Ekaid, A.L. Numerical Study Of Turbulent Natural Convection In An Enclosure With Localized Heating From Left Side. *Eng. Technol. J.* **2009**, *27*, 2692–2710. [CrossRef]
16. Saeid, N.H.; Mohamad, A.A. Periodic free convection from a vertical plate in a saturated porous medium, non-equilibrium model. *Int. J. Heat Mass Transf.* **2005**, *48*, 3855–3863. [CrossRef]
17. Trilok, G.; Kumar, K.K.; Gnanasekaran, N.; Mobedi, M. Numerical assessment of thermal characteristics of metal foams of orderly varied pore density and porosity under different convection regimes. *Int. J. Therm. Sci.* **2022**, *172*, 107288. [CrossRef]
18. Taylor, J.R.; Thompson, W. An Introduction to Error Analysis: The Study of Uncertainties in Physical Measurements. *Phys. Today* **1998**, *51*, 57–58. [CrossRef]
19. Moffat, R.J. Describing the uncertainties in experimental results. *Exp. Therm. Fluid Sci.* **1988**, *1*, 3–17. [CrossRef]
20. Saleh, A.A.M.; Rasheed, S.A.; Smasem, R.B. Convection heat transfer in a channel of different cross section filled with porous media. *Kufa J. Eng.* **2018**, *9*, 57–73. [CrossRef]

21. Fadhil, A.A.; Jumaah, I.D.; Mahbubul, I.; Hasannuzaman, M. Effect of Hump Configurations of Porous Square Cavity on Free Convection Heat Transfer. *Diyala J. Eng. Sci.* **2023**, 1–13. [CrossRef]
22. Lin, W.; Xie, G.; Yuan, J.; Sundén, B. Comparsion and Analysis of Heat Transfer in a Porous Aluminum Foam Using Local Thermal Equilibrium and Local Thermal Non-equilibrium Models. In Proceedings of the 2nd International Workshop on Heat Transfer Advances for Energy Conservation and Pollution Control, Xi'an, China, 18–21 October 2013.
23. Camacho Hernandez, J.N.; Link, G.; Schubert, M.; Hampel, U. Novel Mixing Relations for Determining the Effective Thermal Conductivity of Open-Cell Foams. *Materials* **2022**, *15*, 2168. [CrossRef] [PubMed]
24. Hsieh, W.; Chang, K. Calculation of wall heat transfer in pipeexpansion turbulent flows. *Int. J. Heat Mass Transf.* **1996**, *39*, 3813–3822. [CrossRef]
25. Nie, X.; Zhu, Z.; Liao, H.; Lü, M.; Xu, J. A comparative study of heat transfer characteristics of wall jet with boundary layer transition using six low-Reynolds number *k*–ε models. *AIP Adv.* **2021**, *11*, 025025. [CrossRef]
26. Andreozzi, A.; Buonomo, B.; Jaluria, Y.; Manca, O. Numerical Investigation on Natural Convection in Inclined Channels Partially Filled With Asymmetrically Heated Metal Foam. *ASME J. Heat Mass Transf.* **2023**, *145*, 042602. [CrossRef]
27. Calmidi, V.V. Transport Phenomena in High Porosity Metal Foams. Ph.D. Thesis, University of Colorado, Boulder, CO, USA, 1998.
28. Mahjoob, S.; Vafai, K. A synthesis of fluid and thermal transport models for metal foam heat exchangers. *Int. J. Heat Mass Transf.* **2008**, *51*, 3701–3711. [CrossRef]
29. Bar-Cohen, A.; Rohsenow, W.M. Thermally Optimum Spacing of Vertical, Natural Convection Cooled, Parallel Plates. *J. Heat Transf.* **1984**, *106*, 116–123. [CrossRef]
30. Marcondes, F.; Melo, V.d.S.; Gurgel, J.M. Numerical analysis of natural convection in parallel, convergent, and divergent open-ended channels. *Int. J. Numer. Methods Heat Fluid Flow* **2006**, *16*, 304–323. [CrossRef]


**Disclaimer/Publisher's Note:** The statements, opinions and data contained in all publications are solely those of the individual author(s) and contributor(s) and not of MDPI and/or the editor(s). MDPI and/or the editor(s) disclaim responsibility for any injury to people or property resulting from any ideas, methods, instructions or products referred to in the content.